



of under-coordinated surface sites in nanostructured supports as well as the flexibility of nanoparticles to relax around oxygen vacancies and thereby stabilize them.<sup>18</sup> Several groups have focused on developing nanostructured CeO<sub>2</sub> supports to produce highly defective materials, including by controlling the shape of the nanoparticles,<sup>7,8</sup> template syntheses,<sup>19</sup> and using specific calcination protocols.<sup>9</sup> The addition of supported metal nanoparticles can increase the reducibility of the support by providing an electron sink to stabilize the charge produced by oxygen-vacancy generation.<sup>18</sup> In addition to altering the reducibility of the oxide, deposition also introduces Cu||CeO<sub>2</sub> interfaces that are implicated in reactivity.<sup>20</sup> The aerogel expression of the reducing oxide offers critical attributes: increased reducibility of the support through nanostructuring and more oxide NP||Cu NP junctions.

We now show that another reducible metal oxide aerogel stabilizes metallic Cu. Using CeO<sub>2</sub>, a reducible metal oxide amenable to aerogel synthesis, we report herein that Cu/CeO<sub>2</sub> aerogel stabilizes a significant fraction of reduced Cu species (Cu<sup>0</sup> and Cu<sup>+</sup>) in the Cu nanoparticles. Furthermore, copper nanoparticle-modified ceria aerogel exhibits an SPR and demonstrates high activity for the low-temperature heterogeneous catalytic oxidation of carbon monoxide (CO).

## 2. Results and discussion

### 2.1 Synthesis of Cu/CeO<sub>2</sub> materials

The ceria aerogel (CeO<sub>2</sub>(aero)) is prepared following literature procedures for sol-gel synthesis and then supercritically drying the wet gel.<sup>21</sup> The gel is formed by epoxide-driven hydrolysis of CeCl<sub>3</sub> in methanol. After forming dispersed CeO<sub>2</sub> particles (the “sol”), the hydrolysis continues to covalently crosslink the oxide nanoparticles to form a gel. The aged gel is rinsed with isopropanol and acetone, and then the acetone-filled gel is dried with supercritical CO<sub>2</sub> to produce an amorphous CeO<sub>2</sub>(aero). The aerogel is calcined in static air at 500 °C for 2 h (5 °C min<sup>-1</sup> heating and cooling ramp) to crystallize the networked CeO<sub>2</sub> domains. Post-calcination, CeO<sub>2</sub>(aero) has an average of 82(11) m<sup>2</sup> g<sup>-1</sup> surface area, 0.35(7) cm<sup>3</sup> g<sup>-1</sup> pore volume, and 17(3) nm average pore diameter (Table S1, Fig. S1 and S2†). As is typical for sol-gel syntheses, slight variation occurs between nominally identical batches of the aerogel support; we report

values that are an average of 7 replicate batches. The fluorite crystal structure expected for CeO<sub>2</sub> after calcination at 500 °C is confirmed using powder X-ray diffraction (XRD). Scherrer analysis estimates 6–9 nm diameter crystallites from the (111) reflection at  $2\theta = 28.55^\circ$  (Fig. S3†), with the range reflecting batch-to-batch variation, in good agreement with the highly textured morphology seen by scanning electron microscopy (SEM, Fig. 1).

In order to determine the effects of the aerogel morphology on the properties of the CeO<sub>2</sub> support, we examined a commercially obtained particulate nanopowder ceria (CeO<sub>2</sub>(partic)). The commercial CeO<sub>2</sub> has lower surface area (26 m<sup>2</sup> g<sup>-1</sup> vs. 82(11) m<sup>2</sup> g<sup>-1</sup>) and pore volume (0.09 cm<sup>3</sup> g<sup>-1</sup> vs. 0.35(7) cm<sup>3</sup> g<sup>-1</sup>) than the aerogel and lacks the covalent bonding between CeO<sub>2</sub> nanoparticles present in the aerogel network. Crystalline regions averaged 21(1) nm diameter by XRD, suggesting particulate CeO<sub>2</sub> is 2–3 times larger than the bonded CeO<sub>2</sub> nanoparticles in the aerogel network. By SEM, particles as large as 75 nm across are observed (Fig. 1), which may comprise several crystalline domains or reflect the size range of crystallites in CeO<sub>2</sub>(partic).

Ceria has a direct band gap with an energy ( $E_g$ ) that depends on crystallite size;<sup>22</sup> the energies for CeO<sub>2</sub>(aero) and CeO<sub>2</sub>(partic) are calculated from Tauc plots of the diffuse-reflectance UV-Vis spectra (Fig. S4†). The values are 2.95 eV (420 nm) and 3.08 eV (403 nm) for CeO<sub>2</sub>(aero) and CeO<sub>2</sub>(partic), respectively. Although the CeO<sub>2</sub>(aero) crystallite size is less than the CeO<sub>2</sub> Bohr radius (7–9 nm) and quantum confinement has been observed for dispersed CeO<sub>2</sub> nanoparticles,<sup>23</sup> the covalent attachment of the CeO<sub>2</sub> crystallites in the aerogel framework likely prevents confinement. Indeed, the opposite effect is instead observed, with CeO<sub>2</sub>(aero) showing a decrease in bandgap energy compared to bulk CeO<sub>2</sub> (3.19 eV, 389 nm). This red-shift was previously observed and attributed to the presence of surface Ce ions (in either the 4+ or 3+ oxidation states) and the presence of oxygen vacancies.<sup>24</sup> The red-shift of the bandgap energy for CeO<sub>2</sub>(aero) relative to CeO<sub>2</sub>(partic) is consistent with this interpretation, given the smaller size of the crystallites and higher surface area of the aerogel.

Copper nanoparticles are photodeposited using a modification of the procedure described by Wu *et al.*<sup>25</sup> A slurry of ethanol, water, ceria, and copper(II) nitrate at pH 9–10 is stirred

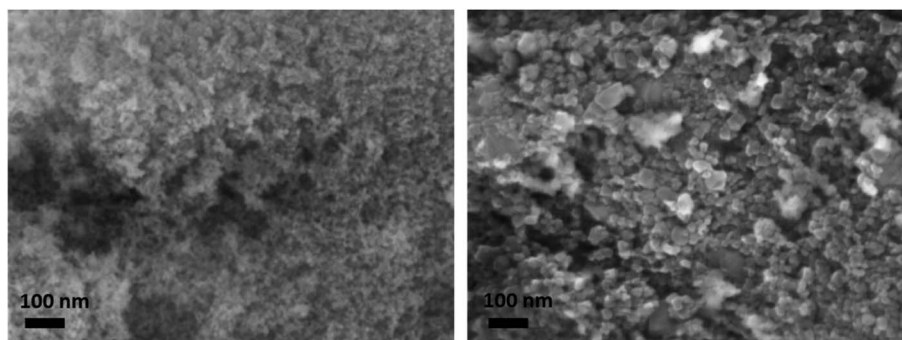


Fig. 1 Scanning electron micrographs of (left) CeO<sub>2</sub>(aero) and (right) CeO<sub>2</sub>(partic).





morphologies. Additional transmission electron micrographs are found in the ESI.†

## 2.2 Influence of support surface area and mesostructure on electronic state of Cu

The diffuse reflectance UV-visible spectra of 5Cu/CeO<sub>2</sub>(aero) and 2.5Cu/CeO<sub>2</sub>(aero) (Fig. 4A and B), prepared with 48 h of irradiation, both exhibit a broad feature at 740 nm consistent with Cu SPR.<sup>6</sup> Irradiation of 5Cu/CeO<sub>2</sub>(partic) did not produce an SPR, despite using the same photodeposition conditions, and instead displayed features consistent with CuO and Cu<sub>2</sub>O.<sup>6</sup> At a higher weight loading, even 96 h of photoreduction does

not produce a visible SPR for 10Cu/CeO<sub>2</sub>(aero). In contrast, 10Cu/TiO<sub>2</sub>(aero) exhibits a Cu SPR feature after only 24 h of photoreduction. Theoretical work predicts that the presence of a Cu SPR suggests that the Cu NPs are at least 2 nm in diameter.<sup>26</sup>

When comparing Cu SPRs produced at 5 wt% Cu supported on the two metal oxide aerogels, the intensity of the SPR is brighter on TiO<sub>2</sub> than on CeO<sub>2</sub> (Fig. 4C), suggesting more metallic Cu is stabilized on TiO<sub>2</sub>(aero) than CeO<sub>2</sub>(aero). Notably, there is a higher absorbance between 400 nm and 600 nm on 5Cu/CeO<sub>2</sub>(aero) relative to 5Cu/TiO<sub>2</sub>(aero), which may be an indication of more Cu<sup>+</sup> on CeO<sub>2</sub> due to the band-gap adsorption of Cu<sub>2</sub>O at ~580 nm.<sup>27</sup>

Ceria appears less able than TiO<sub>2</sub> to support metallic copper given that (1) longer irradiation times are required to produce SPRs, (2) the SPR response is not as bright on CeO<sub>2</sub> relative to TiO<sub>2</sub>, and (3) an SPR is not observed on CeO<sub>2</sub> aerogels at ≥5 wt% Cu. As the ratio of Cu to CeO<sub>2</sub> surface area increases, either by increasing the copper loading or by decreasing the surface area of the support, SPRs are not observed. Rather, we observe large Cu features in the SEM suggesting that the available sites for Cu nucleation have been exhausted, and that further Cu deposition results in particle growth (Fig. S11–S13†). These large copper particulates interact less extensively with the CeO<sub>2</sub> support (have a lower ratio of interface to bulk volume), which is consistent with their oxidized state.

On a per mass basis, CeO<sub>2</sub> has less available surface area (~80 m<sup>2</sup> g<sup>-1</sup>) than TiO<sub>2</sub> (~150 m<sup>2</sup> g<sup>-1</sup>) to support a given weight loading of Cu NPs. On a per mole basis, however, the surface area of the two metal oxide aerogels is comparable (14 000 m<sup>2</sup> (mol CeO<sub>2</sub>)<sup>-1</sup> to 12 000 m<sup>2</sup> (mol TiO<sub>2</sub>)<sup>-1</sup>). The disparity in atomic weight is highlighted by the fact that 10Cu/TiO<sub>2</sub>(aero) and 5Cu/CeO<sub>2</sub>(aero) both support 12 mol% Cu while 10Cu/CeO<sub>2</sub>(aero) supports 23 mol% Cu. Surface area and available nucleation sites are clearly important considerations as to whether or not the photodeposited material can support a Cu SPR. Further illustrating this surface-area dependence, when nanoparticulate supports rather than aerogel supports of either oxide are utilized, the SPR feature is absent.

In addition to surface-area effects, we use X-ray photoelectron spectroscopy (XPS) to assess if differences in the Ce<sup>4+</sup> : Ce<sup>3+</sup> ratio in the aerogel and nanoparticulate supports contribute to the differences in speciation of supported Cu NPs. In the Ce 3d region (Fig. 5A, 875 to 925 eV), the Ce<sup>4+</sup> signature consists of 6 peaks between 882.6 eV and 916.7 eV while Ce<sup>3+</sup> gives rise to 4 peaks between 880.6 eV and 904.1 eV.<sup>28</sup> Recently published results have shown that with these 10 peaks in the Ce 3d region, small modifications to the peak-fitting procedure can vary the estimated Ce<sup>3+</sup> content from 2.3% to 38.9%.<sup>29</sup> Given the similarity of the Ce peaks in our particulate and aerogel samples, we have elected to not fit this region and qualitatively assert that, at least under vacuum conditions, both supports are dominated by Ce<sup>4+</sup> and have similar Ce<sup>3+</sup> content. The similarity in Ce<sup>3+</sup> content suggests that the differences in Cu speciation that we observe are due more to the surface area and morphology of the support than to their degree of reducibility.

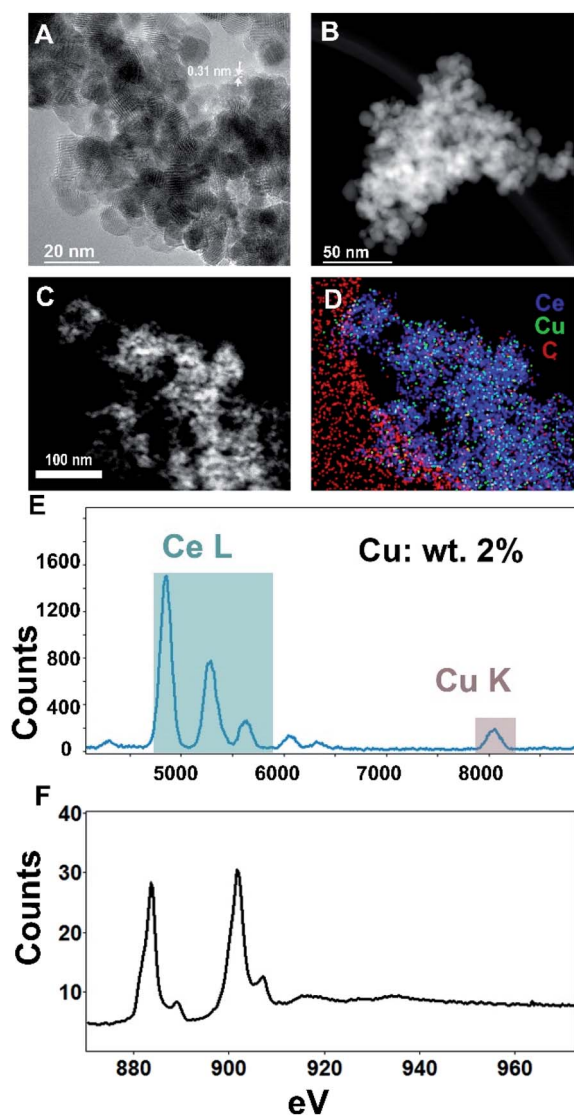


Fig. 3 Transmission electron microscopy (TEM) of copper nanoparticles supported on 5Cu/CeO<sub>2</sub>(aero). (A) High-resolution (HR-TEM) of 5Cu/CeO<sub>2</sub>(aero). (B) High-angle annular dark-field image in scanning mode (STEM-HAADF). (C) STEM-HAADF image corresponding with (D) energy-dispersive spectroscopy in scanning mode (STEM-EDS). (E) EDS plot of broad-beam irradiated 5Cu/CeO<sub>2</sub>(aero) showing Ce and Cu present. (F) Electron energy-loss-spectroscopy of broad-beam irradiated 5Cu/CeO<sub>2</sub>(aero).



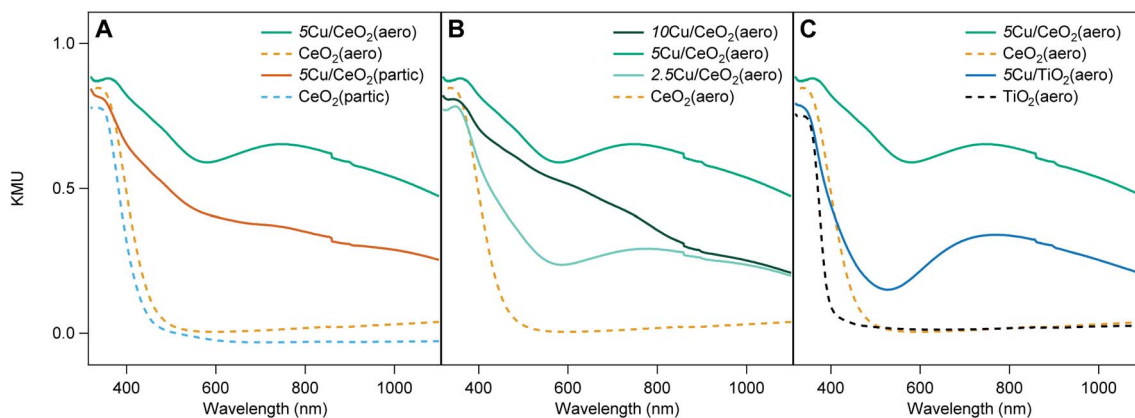


Fig. 4 Diffuse reflectance UV-Vis spectra in Kubelka–Munk units (KMU) for (A) 5Cu/CeO<sub>2</sub>(aero) (green), CeO<sub>2</sub>(aero) (dashed yellow), 5Cu/CeO<sub>2</sub>(partic) (amber), and CeO<sub>2</sub>(partic) (dashed blue); (B) 10Cu/CeO<sub>2</sub>(aero) (dark green), 5Cu/CeO<sub>2</sub>(aero) (green), 2.5Cu/CeO<sub>2</sub>(aero) (light green), and CeO<sub>2</sub>(aero) (dashed yellow); (C) 5Cu/CeO<sub>2</sub>(aero) (green), 5Cu/TiO<sub>2</sub>(aero) (blue), CeO<sub>2</sub>(aero) (dashed yellow), and TiO<sub>2</sub>(aero) (dashed black).

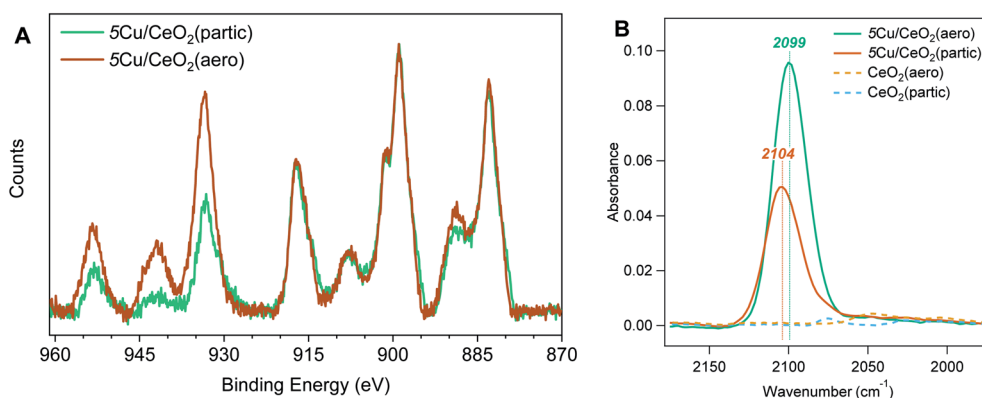


Fig. 5 (A) Background-subtracted X-ray photoelectron spectra of 5Cu/CeO<sub>2</sub>(partic) (amber) and 5Cu/CeO<sub>2</sub>(aero) (green) in the Ce 3d (875 to 925 eV) and Cu 2p (925 to 965 eV) regions. (B) ATR-FTIR spectra for 5Cu/CeO<sub>2</sub>(aero) (green), 5Cu/CeO<sub>2</sub>(partic) (amber), CeO<sub>2</sub>(aero) (dashed yellow), and CeO<sub>2</sub>(partic) (dashed blue), showing CO binding at 2099 cm<sup>-1</sup> and 2104 cm<sup>-1</sup> for 5Cu/CeO<sub>2</sub>(aero) and 5Cu/CeO<sub>2</sub>(partic), respectively.

The differences in Cu speciation between 5Cu/CeO<sub>2</sub>(aero) and 5Cu/CeO<sub>2</sub>(partic) are apparent in the Cu 2p region of the XPS spectra (Fig. 5A, 925 to 965 eV). The Cu 2p<sub>3/2</sub> region consists of a peak at 932 eV for Cu<sup>0</sup> and Cu<sup>+</sup>, low-valent states indistinguishable in these spectra, and a peak at 934 eV for Cu<sup>2+</sup>. Notably, Cu<sup>2+</sup> gives rise to a shake-up feature around 941 eV, which is more prominent for 5Cu/CeO<sub>2</sub>(partic) than 5Cu/CeO<sub>2</sub>(aero). We attempted to resolve Cu<sup>0</sup> and Cu<sup>+</sup> by fitting the Auger CuLMM line; however, given the mixture of oxidation states, peak broadening inherent to insulating materials, and low Cu content of our catalysts, satisfactory fits were not obtained (Fig. S14†).

To quantify the proportion of reduced Cu in these materials (Cu<sup>0</sup> and Cu<sup>+</sup>), we use the method described by Biesinger to compare the area under the 2p<sub>3/2</sub> and shake-up features.<sup>30</sup> The advantage of this method is that it is insensitive to peak broadening caused by surface charging and peak shifts expected for Cu particles of different sizes on supports.<sup>31</sup> We find a higher percentage of reduced Cu for 5Cu/CeO<sub>2</sub>(aero) (50 ±

19%) than for 5Cu/CeO<sub>2</sub>(partic) (30 ± 10%), which is consistent with the presence of an SPR on the aerogel and lack of an SPR on the particulate. For 5Cu/TiO<sub>2</sub>(aero) this method gives 30% reduced Cu, which given the prominence of the SPR, suggests that the reduced Cu is predominantly metallic. In contrast, given its lack of an SPR, the 30% reduced Cu content in 5Cu/CeO<sub>2</sub>(partic) is likely Cu<sup>+</sup>. The signal intensity of Cu (relative to Ce) for 5Cu/CeO<sub>2</sub>(partic) is also higher than for 5Cu/CeO<sub>2</sub>(aero), despite XRF confirming similar Cu loadings. This difference is expected for a support with lower surface area. XPS is a surface-sensitive technique, and a larger fraction of the surface of the low surface-area particulate is covered with Cu at the same mass loading as on the high surface-area aerogel. We observed a similar overestimation by XPS of Cu loading on TiO<sub>2</sub>(partic) supports, which have a surface area of 10 m<sup>2</sup> g<sup>-1</sup>.<sup>32</sup>

We utilize CO as a probe molecule in attenuated total reflectance Fourier transform infrared (ATR-FTIR) spectroscopy to interrogate the morphology and electronic structure of the photodeposited Cu. Binding modes are observed at 2099 cm<sup>-1</sup> and





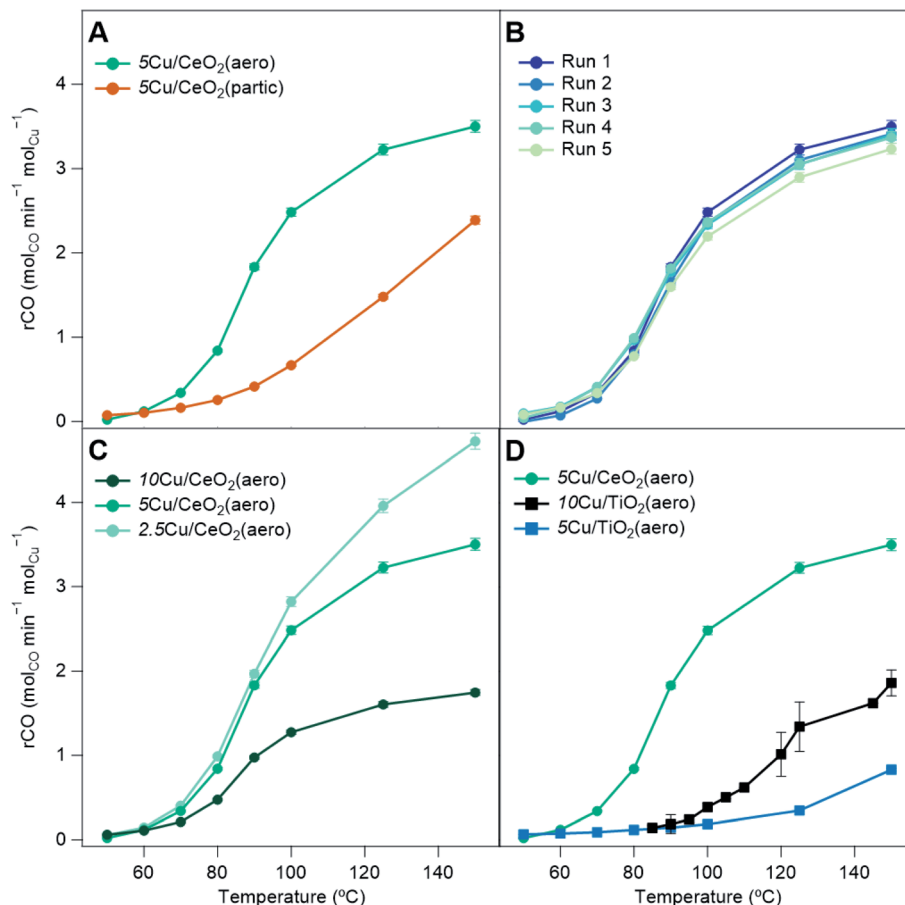


Fig. 6 CO conversion as a fraction of mol CO converted per min per mol Cu in catalyst bed versus temperature for (A) catalysts with different CeO<sub>2</sub> supports: 5Cu/CeO<sub>2</sub>(aero) (green) and 5Cu/CeO<sub>2</sub>(partic) (amber); (B) 5 runs of 5Cu/CeO<sub>2</sub>(aero) separated by regeneration of the catalyst bed; (C) different weight loading of Cu on CeO<sub>2</sub>(aero): 10Cu/CeO<sub>2</sub>(aero) (dark green), 5Cu/CeO<sub>2</sub>(aero) (green), 2.5Cu/CeO<sub>2</sub>(aero) (light green); and (D) catalysts with CeO<sub>2</sub> vs. TiO<sub>2</sub> supports: 5Cu/CeO<sub>2</sub>(aero) (green), 5Cu/TiO<sub>2</sub>(aero) (blue), 10Cu/TiO<sub>2</sub>(aero) (black).

inaccessible or that Cu particles do not contain the appropriate synergistic mixture of Cu<sup>0</sup> and Cu<sup>+</sup> to aid in turnover.

Despite having lower surface area and lower Cu weight loading, 5Cu/CeO<sub>2</sub>(aero) shows higher CO conversion than 10Cu/TiO<sub>2</sub>(aero). When photodepositing Cu, sufficient surface area is required to prevent the formation of Cu aggregates and to ensure the extended interaction between the metal oxide support and the Cu NPs. But with this surface area requirement met in both 5Cu/CeO<sub>2</sub>(aero) and 10Cu/TiO<sub>2</sub>(aero), the superior CO oxidation activity shown on the CeO<sub>2</sub>(aero) supports at a lower Cu weight loading is likely due to the increased reducibility of CeO<sub>2</sub>. The increased reducibility of CeO<sub>2</sub> facilitates generation of oxygen vacancies that activate molecular O<sub>2</sub>.<sup>16–18</sup> Activated oxygen species react with CO bound to Cu<sup>+</sup> sites located near the oxide interface<sup>20</sup> to facilitate CO<sub>2</sub> generation.

### 3. Conclusions

We show that reduced Cu NPs displaying SPRs are supported on high surface-area CeO<sub>2</sub> aerogel, similar to our prior report for Cu supported on TiO<sub>2</sub> aerogel. The high surface area of the support is a critical factor in creating the close contact between

the Cu NPs and the reducing oxide required to stabilize Cu<sup>0</sup>. When the surface area of the support relative to Cu content is lower, either by using a lower surface area support or by increasing Cu loading, the fraction of oxidized Cu is higher, and the Cu SPR is not observed. The consequence of the ability of the CeO<sub>2</sub> morphology to tune activity is seen in the low activity of Cu/CeO<sub>2</sub>(partic) for low-temperature CO oxidation. The Cu/CeO<sub>2</sub>(aero) catalysts far outperform their Cu/TiO<sub>2</sub>(aero) counterparts for low-temperature CO oxidation even at lower Cu weight loadings or equal mole fractions, showing that the transition to the more reducible CeO<sub>2</sub> produces more catalytically active materials. Even with the high surface area CeO<sub>2</sub>(aero), in the absence of Cu, low-temperature CO oxidation is not observed. The generalization of the Cu/MOx(aero) motif for stabilizing reduced states of Cu offers a design principle for reactions that benefit from these low-valent states.

### 4. Experimental

#### 4.1 Materials

Copper(II) nitrate hemipentahydrate (Cu(NO<sub>3</sub>)<sub>2</sub>·2.5H<sub>2</sub>O, Sigma-Aldrich, 98%), cerium chloride heptahydrate (CeCl<sub>3</sub>·7H<sub>2</sub>O,



Sigma-Aldrich, 99.9%), ( $\pm$ )-propylene oxide (Sigma-Aldrich,  $\geq 99\%$ ), ceria nanopowder (Sigma-Aldrich,  $< 50$  nm particles, 99.95%, Lot# MKCD8228), ethanol (absolute ethanol, Warner-Graham), and nitric acid ( $\text{HNO}_3$ , Fisher 69.9%) were used as received. Methanol (Fisher, 99.9%) for  $\text{CeO}_2$  aerogel synthesis was stored over 3 Å sieves and filtered before use. Ultrapure 18 M $\Omega$  cm water (Barnstead Micropure) was used in all syntheses requiring water.

#### 4.2 Synthesis of cerium oxide ( $\text{CeO}_2$ ) aerogels

Cerium oxide aerogels were prepared by a modification of a literature procedure.<sup>21</sup> In a plastic beaker, 2.39 g of  $\text{CeCl}_3 \cdot 7\text{H}_2\text{O}$  (6.4 mmol) was dissolved in 10 g of anhydrous MeOH, followed by adding 6 g of propylene oxide while stirring. The solution was allowed to stir until a gel formed and then covered and aged overnight. The aged gel was transferred to a jar, washed several times with isopropanol and then acetone. The wet gels were loaded into a supercritical dryer under acetone, and the acetone was then exchanged for liquid  $\text{CO}_2$  at 10 °C over the course of several rinses. The temperature of the dryer was raised to 42 °C, forming a supercritical  $\text{CO}_2$  phase and vented slowly to atmospheric pressure. The aerogels were calcined in air at 500 °C (5 °C  $\text{min}^{-1}$  ramp, 2 h dwell, 5 °C  $\text{min}^{-1}$  cooling ramp) to yield nanocrystalline fluorite  $\text{CeO}_2$  aerogel.

#### 4.3 Deposition of Cu nanoparticles at $\text{CeO}_2$ supports

Copper deposition followed a modification of the method used to photodeposit Cu nanoparticles on  $\text{TiO}_2$  aerogels.<sup>6</sup> As an exemplar for 5 wt% Cu loading, a slurry of 100 mg of  $\text{CeO}_2$  aerogel or commercial  $\text{CeO}_2$  (0.27 mmol) and 19 mg of  $\text{Cu}(\text{NO}_3)_2 \cdot 2.5\text{H}_2\text{O}$  (0.08 mmol, 5.2 mg Cu) in 68 mL 9 : 1  $\text{H}_2\text{O}$  : EtOH in a Pyrex round bottom flask was brought to pH  $9.5 \pm 0.5$  with aqueous NaOH and  $\text{HNO}_3$ . The solution was sparged with Ar for 30 min prior to irradiating the sample with a 500 W Xe arc lamp (Newport-Oriel) for 48 h. The solids were collected by filtration (0.1  $\mu\text{m}$  polyvinylidene fluoride membrane filter), washed with several aliquots of water, air-dried overnight, and then dried at 70 °C for 16 h.

#### 4.4 Structural, physical and chemical characterization

The Brunauer–Emmett–Teller (BET) surface area and Barrett–Joyner–Halenda (BJH) pore size distributions were derived from the desorption arm of the  $\text{N}_2$  physisorption isotherms (Micromeritics ASAP2020). The isotherm data were fit with Micromeritics DFTplus software using the Harkins and Jura thickness curve employing the Faas correction. Prior to  $\text{N}_2$  physisorption, samples were degassed at 150 °C for 10 h. The crystalline phases were characterized using X-ray diffraction (Rigaku SmartLab, 40 kV and 44 mA, 4°  $\text{min}^{-1}$  scan rate). The average crystallite diameter was determined *via* the Scherrer equation using the full width half maximum (FWHM) of the  $\text{CeO}_2$  (111) diffraction peak at  $2\theta = 28.55^\circ$ . Diffuse-reflectance UV-visible spectra (PerkinElmer 750, 60 mm integrating sphere) were converted to absorbance using the Kubelka–Munk transformation. Optical band gaps were determined from Tauc plots by extrapolating the linear portion of the plot near the absorption edge to the energy axis. The X-ray photoelectron spectra (Thermo Scientific

K-Alpha, Al-K $\alpha$  radiation) were recorded using a flood gun to minimize charging on the insulating samples. High-resolution spectra were recorded in the Cu 2p, Ce 3d, and O 1s regions. Peak integration was performed with a Smart background on Avantage software. All peak positions were referenced to the  $\text{Ce}^{4+}$  3d $_{3/2}$  shake-up peak at 916.7 eV.<sup>28</sup> The scanning electron micrographs were recorded using a LEO Supra 55 field-emission microscope operating at 10 keV in secondary electron mode. Transmission electron microscopy was performed in a JEOL JEM2200FS operating at 200 kV for HR-TEM, preliminary STEM-HAADF, and STEM-EDS while an aberration-corrected STEM Nion UltraSTEM200X operating at 200 kV was used for additional STEM-HAADF, STEM-EELS, and STEM-EDS. Samples of Cu/ $\text{CeO}_2$  were prepared *via* sonication in isopropyl alcohol with dropcasting onto lacey-carbon supports on gold TEM grids.

#### 4.5 Attenuated total reflectance FTIR (ATR)

We prepared suspensions of  $\text{CeO}_2$  and Cu/ $\text{CeO}_2$  by sonicating 20 mg of sample in 1.0 mL DI water for 15 min and drop cast 2  $\mu\text{L}$  of each sample onto a ZnSe ATR prism for a loading of 4 mg. To increase wettability of the ZnSe ATR prisms prior to drop casting, we plasma oxidized the clean prism under 310 mTorr and 250 mL  $\text{min}^{-1}$   $\text{O}_2$  for 5 min (March Fluorine Reactive Ion Etcher). The ATR spectra were monitored with a Nicolet 6700 (ThermoFisher) equipped with a liquid nitrogen-cooled MCT/B detector. Spectra were taken during the fill as well as purging segments with a resolution of 4  $\text{cm}^{-1}$  in the range of 650–4000  $\text{cm}^{-1}$  as a product of a 32-scan average with no attenuation and an aperture setting to 74%.

The binding of CO on  $\text{CeO}_2$  and Cu/ $\text{CeO}_2$  was investigated at room temperature under anaerobic conditions (10 mL  $\text{min}^{-1}$  CO, 25 mL  $\text{min}^{-1}$  He). The sample was dried overnight under He flow prior to CO exposure. The feed stream flowed over the sample for 10 min to saturate the catalyst surface, then  $\text{CO}_{(\text{g})}$  was purged from the system with 25 mL  $\text{min}^{-1}$  He for 5 h.

#### 4.6 Carbon monoxide oxidation

Carbon monoxide (CO) oxidation was performed in a glass tube (3/8" OD, 0.22" ID) continuous-flow packed bed reactor (PBR) housed in a programmable ceramic tube oven. Reactions were conducted under dark conditions. The temperature controller (Digi-Sense 1-Zone, Cole Parmer) was interfaced to a K-type thermocouple affixed to the outer wall of the reactor. The temperature differential between the center of the catalyst bed and the outer wall of the reactor is a possible source of error; however, the thin, 0.15", glass-tube reactor wall should not be sufficient to generate a significant temperature gradient. Reaction conditions were chosen such that heat and mass transport effects were inconsequential.<sup>32,37,38</sup> The 50 mg catalyst bed was sandwiched between glass wool. We diluted 10 mg of Cu/ $\text{CeO}_2$  catalyst with 40 mg of native (*i.e.*, Cu-free)  $\text{CeO}_2$  in order to increase space time and limit conversion.

Prior to reaction, the catalyst bed was activated at 150 °C (ramp rate 10 °C  $\text{min}^{-1}$ , dwell time 30 min) in an anoxic gas stream of 1.25% CO in He (64 mL  $\text{min}^{-1}$ ). These conditions were chosen to minimize ripening, to highlight the ability of the



catalyst to function without high-temperature oxidation and reduction treatments, and to facilitate comparison to earlier work.<sup>32,35,39</sup> During reaction, the reactor was kept at atmospheric pressure while feeding 80 mL min<sup>-1</sup> of 1% CO (Airgas, 10 000 ppm), 20% O<sub>2</sub> (Keen, 4.4 grade, 200 000 ppm), and 79% He (Praxair, 5.0 UHP), giving a GHSV of 39 000 h<sup>-1</sup>. The temperature was decreased stepwise at a ramp rate of 2 °C min<sup>-1</sup>. Reactor effluent was fed into an in-line GC (GC-2014, Shimadzu) equipped with a Pulsed Discharge Detector for product analysis. Reaction products were analyzed at steady state by allowing the reactor to dwell at each temperature (150 °C, 125 °C, 100 °C, 90 °C, 80 °C, 70 °C, 60 °C, and 50 °C) for 35 min. The durability and aging of the catalyst was tested *via* four regenerations for a total of 5 cycles.

## Conflicts of interest

The authors have no conflicts of interest to declare.

## Acknowledgements

The authors acknowledge funding provided by the Office of Naval Research and the Defense Threat Reduction Agency (DTRA, HDTRA1825787). C. L. P. and A. M. P. gratefully acknowledge the National Research Council for support through a Naval Research Laboratory/National Research Council Postdoctoral Associateship.

## References

- 1 A. E. Baber, X. Yang, H. Y. Kim, K. Mudiyansele, M. Soldemo, J. Weissenrieder, S. D. Senanayake, A. Al-Mahboob, J. T. Sadowski, J. Evans, J. A. Rodriguez, P. Liu, F. M. Hoffmann, J. G. Chen and D. J. Stacchiola, *Angew. Chem., Int. Ed.*, 2014, **53**, 5336–5340, DOI: 10.1002/anie.201402435.
- 2 S. D. Senanayake, N. A. Pappoe, T.-D. Nguyen-Phan, S. Luo, Y. Li, W. Xu, Z. Liu, K. Mudiyansele, A. C. Johnston-Peck, A. I. Frenkel, I. Heckler, D. Stacchiola and J. A. Rodriguez, *Surf. Sci.*, 2016, **652**, 206–212, DOI: 10.1016/j.susc.2016.02.014.
- 3 D. Vovchok, C. J. Guild, J. Llorca, W. Xu, T. Jafari, P. Toloueinia, D. Kriz, I. Waluyo, R. M. Palomino, J. A. Rodriguez, S. L. Suib and S. D. Senanayake, *Phys. Chem. Chem. Phys.*, 2017, **19**, 17708–17717, DOI: 10.1039/c7cp02378b.
- 4 Y. Bu, S. Er, J. W. Niemantsverdriet and H. O. A. Frederiksson, *J. Catal.*, 2018, **357**, 176–187, DOI: 10.1016/j.jcat.2017.11.014.
- 5 Y. Zhang, L. Liang, Z. Chen, J. Wen, W. Zhong, S. Zou, M. Fu, L. Chen and D. Ye, *Appl. Surf. Sci.*, 2020, **516**, 146035, DOI: 10.1016/j.apsusc.2020.146035.
- 6 P. A. DeSario, J. J. Pietron, T. H. Brintlinger, M. McEntee, J. F. Parker, O. Baturina, R. M. Stroud and D. R. Rolison, *Nanoscale*, 2017, **9**, 11720–11729, DOI: 10.1039/c7nr04805j.
- 7 D. Gamarra, A. López Cámara, M. Monte, S. B. Rasmussen, L. E. Chinchilla, A. B. Hungria, G. Munuera, N. Gyorffy, Z. Schay, V. Cortés Corberán, J. C. Conesa and A. Martínez-Arias, *Appl. Catal., B*, 2013, **130–131**, 224–238, DOI: 10.1016/j.apcatb.2012.11.008.
- 8 M. Lykaki, E. Pachatouridou, S. A. C. Carabineiro, E. Iliopoulou, C. Andriopoulou, N. Kallithrakas-Kontos, S. Boghosian and M. Konsolakis, *Appl. Catal., B*, 2018, **230**, 18–28, DOI: 10.1016/j.apcatb.2018.02.035.
- 9 C. Wang, Q. Cheng, X. Wang, K. Ma, X. Bai, S. Tan, Y. Tian, T. Ding, L. Zheng, J. Zhang and X. Li, *Appl. Surf. Sci.*, 2017, **422**, 932–943, DOI: 10.1016/j.apsusc.2017.06.017.
- 10 L. Du, W. Wang, H. Yan, X. Wang, Z. Jin, Q. Song, R. Si and C. Jia, *J. Rare Earths*, 2017, **35**, 1186–1196, DOI: 10.1016/j.jre.2017.04.005.
- 11 R. Si, J. Raitano, N. Yi, L. Zhang, S.-W. Chan and M. Flytzani-Stephanopoulos, *Catal. Today*, 2012, **180**, 68–80, DOI: 10.1016/j.cattod.2011.09.008.
- 12 X. Wang, J. A. Rodriguez, J. C. Hanson, D. Gamarra, A. Martínez-Arias and M. Fernández-García, *J. Phys. Chem. B*, 2006, **110**, 428–434, DOI: 10.1021/jp055467g.
- 13 K. Mudiyansele, S. D. Senanayake, L. Faria, S. Kundu, A. E. Baber, J. Graciani, A. B. Vidal, S. Agnoli, J. Evans, R. Chang, S. Axnanda, Z. Liu, J. F. Sanz, P. Liu, J. A. Rodriguez and D. J. Stacchiola, *Angew. Chem., Int. Ed.*, 2013, **52**, 5101–5105, DOI: 10.1002/anie.201210077.
- 14 D. Delimaris and T. Ioannides, *Appl. Catal., B*, 2009, **89**, 295–302, DOI: 10.1016/j.apcatb.2009.02.003.
- 15 C. Hu, Q. Zhu, Z. Jiang, Y. Zhang and Y. Wang, *Microporous Mesoporous Mater.*, 2008, **113**, 427–434, DOI: 10.1016/j.micromeso.2007.11.043.
- 16 M. Konsolakis, *Appl. Catal., B*, 2016, **198**, 49–66, DOI: 10.1016/j.apcatb.2016.05.037.
- 17 A. Migani, G. N. Vayssilov, S. T. Bromley, F. Illas and K. M. Neyman, *Chem. Commun.*, 2010, **46**, 5936–5938, DOI: 10.1039/c0cc01091j.
- 18 A. R. Puigdollers, P. Schlexer, S. Tosoni and G. Pacchioni, *ACS Catal.*, 2017, **7**, 6493–6513, DOI: 10.1021/acscatal.7b01913.
- 19 Y. Su, Z. Tang, W. Han, Y. Song and G. Lu, *Catal. Surv. Asia*, 2015, **19**, 68–77, DOI: 10.1007/s10563-015-9185-3.
- 20 A. Chen, X. Yu, Y. Zhou, S. Miao, Y. Li, S. Kuld, J. Sehested, J. Liu, T. Aoki, S. Hong, M. F. Camellone, S. Fabris, J. Ning, C. Jin, C. Yang, A. Nefedov, C. Wöll, Y. Wang and W. Shen, *Nat. Catal.*, 2019, **2**, 334–341, DOI: 10.1038/s41929-019-0226-6.
- 21 C. Laberty-Robert, J. W. Long, E. M. Lucas, K. A. Pettigrew, R. M. Stroud, M. S. Doescher and D. R. Rolison, *Chem. Mater.*, 2006, **18**, 50–58, DOI: 10.1021/cm051385t.
- 22 V. Ramasamy and G. Vijayalakshmi, *Mater. Sci. Semicond. Process.*, 2016, **42**, 334–343, DOI: 10.1016/j.mssp.2015.10.026.
- 23 N. S. Arul, D. Mangalaraj, P. C. Chen, N. Ponpandian and C. Viswanathan, *Mater. Lett.*, 2011, **65**, 2635–2638, DOI: 10.1016/j.matlet.2011.05.022.
- 24 A. Corma, P. Atienzar, H. García and J.-Y. Chane-Ching, *Nat. Mater.*, 2004, **3**, 394–397, DOI: 10.1038/nmat1129.
- 25 G. J. Wu, N. J. Guan and L. D. Li, *Catal. Sci. Technol.*, 2011, **1**, 601–608, DOI: 10.1039/c1cy00036e.



